Chemical Engineering Journal 499 (2024) 156590

Contents lists available at ScienceDirect

Chemical Engineering Journal

journal homepage: www.elsevier.com/locate/cej

Li-vacant topotactic subsurface Pathways: A Key to stable Li-ion storage and migration in $LiNi_{0.5}Mn_{1.5}O_4$ Cathodes

Taekyun Jeong [a], Sungkyoung Kang [b], Seonguk Lim [a], Sieun An [c], Chungsun Oh [c], Jun-Ho Park [d,e,*], Dongwook Han [c,*]

[a] School of Nano Convergence Technology, Hallym University, 1 Hallymdaehak-gil, Chuncheon 24252, Republic of Korea
[b] Department of Chemistry, Korea Advanced Institute of Science and Technology (KAIST), 291 Daehak-ro, Yuseong-gu, Daejeon 34141, Republic of Korea
[c] Department of Future Energy Convergence, Seoul National University of Science and Technology, 232 Gongneung-ro, Nowon-gu, Seoul 01811, Republic of Korea
[d] Battery Materials and Process Research Center, Battery Research Division, Korea Electrotechnology Research Institute (KERI), 12 Jeongiui-gil, Seongsan-gu, Changwon 51543, Republic of Korea
[e] Department of Electro-Functionality Materials Engineering, University of Science and Technology (UST), Daejeon 34113, Republic of Korea

ARTICLE INFO

Keywords:
Li-vacant topotactic subsurface
Potassium hydroxide
Superior Li-ion kinetics
Outstanding structural integrity
Lithium nickel-manganese oxides
Lithium-ion rechargeable batteries

ABSTRACT

High-voltage $LiNi_{0.5}Mn_{1.5}O_4$ (LNMO) with a spinel structure holds great promise for enhancing the performance of Li-ion rechargeable batteries (LIBs) in the mobility industry. A critical challenge remains in stabilizing Li-ion storage and migration within these cathode materials. Surface engineering emerges as a pivotal technology, significantly influencing the chemical status of LNMO particle surfaces through the application of specific functional materials. In this study, we present a novel synthesis of disordered spinel LNMO cathode materials (space group: Fd-3 m) featuring a Li-vacant topotactic subsurface and an external surface modified with K_2CO_3, achieved via a KOH-assisted wet chemistry approach. The LNMO particles are categorized into three distinct regions based on two compositional boundaries: bulk, (inner) subsurface, and (external) surface. The delithiated subsurface exhibits an intensified ordered arrangement of Ni and Mn, minimizing the formation of detrimental impurity phases while promoting efficient Li-ion transport throughout the spinel lattice. Furthermore, the incorporation of K_2CO_3 provides chemical protection to the external surfaces of LNMO particles, effectively mitigating H_2O adsorption and oxidative electrolyte decomposition. These synergistic effects culminate in remarkable electrochemical performance (reversible discharge capacity: ~110 mA h/g at a current density of 0.2C; discharge capacity retention: ~97 % after 100 cycles) and thermal stability of LNMO, offering significant insights for the advancement of superior high-voltage cathode materials for next-generation LIBs.

1. Introduction

In today's context, reducing both costs and the risk of explosions is indispensable for the widespread adoption of Li-ion rechargeable batteries (LIBs) in the mobility industry [1,2]. In particular, the Co– and Ni-rich cathode materials commonly employed in commercial LIBs, such as $LiCoO_2$ and $LiNi_xCo_yMn_{1-x-y}O_2$ ($x \geq 0.5$) with a layered crystal structure, face challenges arising from the increasing costs of raw materials and insufficient thermal stability [3–7]. Hence, Mn-rich $LiNi_xMn_{2-x}O_4$ ($x = 0$, 0.5) with a spinel structure is increasingly preferred as a cathode material for large-scale LIBs due to its low material costs and exceptional structural integrity at elevated temperatures [8–10].

In terms of operating voltage, the two promising compositions, $LiMn_2O_4$ (LMO) and $LiNi_{0.5}Mn_{1.5}O_4$ (LNMO), are simply divided into 4 V- and 5 V-class spinel compounds, respectively. Despite having nearly identical theoretical capacities, LMO and LNMO exhibit a substantial disparity in energy density, which is attributed to the notable difference in their operating voltage (LMO: ~4 V, LNMO: ~4.7 V vs. Li^+/Li) [11–13]. In addition, LMO, characterized by a high content of high-spin Mn^{3+} ions, undergoes significant crystal structure distortion induced by the Jahn-Teller effect and experiences the dissolution of Mn^{2+} ions from the surface of LMO particles into the electrolyte through a disproportionation reaction ($2Mn^{3+} \rightarrow Mn^{2+} (\downarrow) + Mn^{4+}$) [14,15].

Conversely, LNMO is predominantly composed of electrochemically

* Corresponding authors at: Department of Future Energy Convergence, Seoul National University of Science & Technology, 232 Gongneung-ro, Nowon-gu, Seoul 01811, Republic of Korea (D. Han).
E-mail addresses: junhopark@keri.re.kr (J.-H. Park), dw.han@seoultech.ac.kr (D. Han).

https://doi.org/10.1016/j.cej.2024.156590

Available online 10 October 2024

inactive Mn^{4+} and active Ni^{2+} ions. Therefore, LNMO benefits from a lower content of Jahn-Teller active Mn^{3+} ions, which helps in avoiding pronounced lattice distortion during charging and discharging [16,17]. The consecutive redox reactions of Ni^{3+}/Ni^{2+} and Ni^{4+}/Ni^{3+} with a high operating voltage exceeding 4.7 V enable the realization of LIBs that combine LNMO with high-voltage anode materials like $Li_4Ti_5O_{12}$ (LTO). During electrochemical cycling, LTO exhibits a voltage plateau at ~ 1.5 V, accompanied by minimal distortion (i.e., zero-strain) in its spinel structure and negligible electrolyte decomposition under reduction conditions [18–20]. In this context, LNMO/LTO full cells with an operating voltage of ~ 3.2 V can offer high power and exceptional safety, owing to the inherent 3D Li-ion diffusion pathways and robust structural stability of their spinel structures.

Nevertheless, unlike LMO, the commercialization of LNMO continues to face obstacles due to the formation of an unstable interface between LNMO particles and the electrolyte, especially in high-voltage regions [21,22]. Typical conventional organic electrolytes employed in LIBs are susceptible to decomposition through their oxidation reactions in these regions. This undesirable process leads to the formation of thick, poorly conductive cathode-electrolyte interface (CEI) layers on the LNMO particles, thereby impeding the transfer of Li^+ ions across these layers [23,24]. Furthermore, the electrochemical instability of LNMO surfaces at high states of charge induces structural deterioration and the dissolution of transition metals (Ni, Mn), subsequently accelerating the capacity degradation of LNMO during cycling [25–27].

To improve the cycling performance of LNMO under high-voltage conditions, ongoing research includes optimizing synthetic processes [28–31], chemical compositions [32–34], and particle morphologies [35,36] for LNMO, as well as developing compatible electrolytes and additives with superior oxidation resistance [37,38]. Moreover, considering the severe deformation of the spinel structure and the formation of low-conductive CEI layers on the surfaces of LNMO particles, it is indispensable to protect these surfaces from direct contact with the electrolyte. Indeed, a variety of functional materials, such as metallic, carbon-based, and lithiated compounds, have proven effective when applied to the LNMO surfaces [39–42]. The proposed coating materials can enhance the chemical stability and electrical/ionic conductivities at the LNMO/electrolyte interfaces based on their functionality. However, as the content of these materials increases, the gravimetric and volumetric capacities of LNMO tend to diminish due to the increased accumulation of electrochemically inactive coating layers on its surfaces. Additionally, typical surface coating technologies are ineffective in directly altering the chemical status in the immediate internal region around LNMO surfaces, known as the (inner) subsurface, because they predominantly affect the exterior of particle surfaces [10]. These inadequate techniques encompass mechanical dry coating methods as well as chemical wet processes, including co-precipitation, sol–gel, chemical vapor deposition (CVD), and atomic layer deposition (ALD) [39].

Hence, we considered a novel process to simultaneously modify the chemical bond structure on the external surface and the chemical composition in the subsurface of LNMO. To achieve this, an aqueous solution of potassium hydroxide (KOH) was introduced as a chemical reagent to alter both the surface configuration and subsurface chemistry of LNMO. First, hydroxide ions (OH^-) adsorbed on the external surface of LNMO particles can selectively extract Li^+ ions from the bulk of LNMO while preventing the dissolution of Ni and Mn into the aqueous solution [43–45]. When the identical procedure is conducted in acid environments, the ionic exchange between H^+ and Li^+ ions leads to substantial metal dissolution, thereby disrupting the pristine spinel framework of the LNMO bulk [46,47]. Lu et al. recently proposed $La(OH)_3$ as a Li-ion capturer to enhance the surface stability of Ni-rich layered oxide cathode materials [48]. This reconstructed surface, consisting of a delithiated epitaxial layer and Li-ion conductive $LiLaO_2$ nanoparticles, alleviated the reactivity between the cathode oxides and organic electrolytes. Second, KOH chemically produces thermally stable potassium carbonate (K_2CO_3) on hydrated active surfaces by reacting with CO_2 molecules dissolved in a KOH solution via a CO_2 capture reaction ($2KOH + CO_2 \rightarrow K_2CO_3 + H_2O$) [49]. Specifically, the adsorption of K^+ ions onto the surface of hydrated LNMO particles is preferred over H_2O adsorption, as it reduces surface energy [50]. In addition, we anticipated that the pre-existing K_2CO_3 component would inhibit the thickening of CEI layers during cycling and facilitate Li-ion migration by providing more conductive channels compared to Li_2CO_3, the main inorganic component of typical CEI layers [51,52].

In this study, we first developed LNMO cathode materials featuring a Li-vacant topotactic subsurface through a KOH-assisted wet chemistry method. This approach resulted in improved Li-ion kinetics and storage properties in the bulk of LNMO particles, attributed to the delithiated subsurface and the K_2CO_3-enriched external surface (Scheme 1). Furthermore, these synergistic effects not only eliminated detrimental secondary phases (e.g., $Li_xNi_{1-x}O$) and adsorbed H_2O molecules, but also mitigated thermal degradation within the LNMO lattice.

2. Experimental

2.1. Material preparation

$LiNi_{0.5}Mn_{1.5}O_4$ (LNMO) cathode materials were synthesized via co-precipitation-assisted hydrothermal followed by solid-state reactions. For the synthesis of referenced LNMO (referred to as R-LNMO), we prepared "Solution A" by homogenously mixing $NiSO_4{\cdot}6H_2O$ (0.3942 g) and $MnSO_4{\cdot}H_2O$ (0.7605 g) in deionized (DI) water (45 mL) with continuous stirring for 15 min. "Solution B" was prepared by adding NH_4HCO_3 (0.711 g) to DI water (15 mL) and stirred for 10 min. Subsequently, co-precipitation reactions were initiated by dropping Solution B into Solution A. Throughout the entire process, N_2 bubbling was employed to prevent the oxidation of transition metals (Ni, Mn). A green solution observed during the co-precipitation reactions served as evidence for the divalent state of Ni ions [53]. The co-precipitated green solution was carefully transferred into a Teflon-lined autoclave (100 mL) and then maintained at a temperature of 200 ℃ for 32 h. After the hydrothermal reactions were completed, the autoclave reactor was gradually cooled to room temperature (RT) in ambient air. Following centrifugation, a high-purity product (i.e., metal carbonate with a Ni to Mn atomic ratio of 1:3) was obtained through washing with DI water and ethanol to remove residual sulfate radicals. It was then moved into a vacuum oven and dried at 120 ℃ for 12 h. Finally, the metal carbonate, utilized as the metal precursor for the R-LNMO synthesis, was converted into a metal oxide by heating it at 500 ℃ for 2 h under a flow of air gas (2 L/min). Then, stoichiometric amounts of the metal oxide and Li_2CO_3 were uniformly mixed using a double shaking mixer. At this time, we added 5 wt% excess of the Li_2CO_3 precursor to the mixture to compensate for the Li loss upon heating at high temperatures. The precursor mixture was crystallized into R-LNMO via consecutive heating at 400 ℃ for 2 h, 600 ℃ for 2 h, and 800 ℃ for 3 h under a flow of air gas (2 L/min).

To prepare surface-modified LNMO (referred to as LNMO_KOH), R-LNMO was uniformly dispersed and stirred in a KOH (1.25 M) aqueous solution for 30 min. N_2 bubbling was employed throughout the dispersion to prevent the oxidation of transition metals in R-LNMO. Finally, LNMO_KOH was obtained by washing the KOH-treated LNMO with DI water, followed by drying it in a vacuum oven at 120 ℃ for 12 h. The overall synthesis processes for R-LNMO and LNMO_KOH are depicted in Fig. 1.

2.2. Physicochemical characterization

The crystal structures of the (Ni, Mn) carbonate precursor, R-LNMO, and LNMO_KOH samples were analyzed via X-ray diffraction (XRD; X'Pert PRO MPD, PANalytical) using Cu Ka radiation ($\lambda = 1.5406$ Å) with a 2θ range spanning 15° to 75°. Ex-situ XRD analyses were performed on R-LNMO and LNMO_KOH after 100 charge/discharge cycles

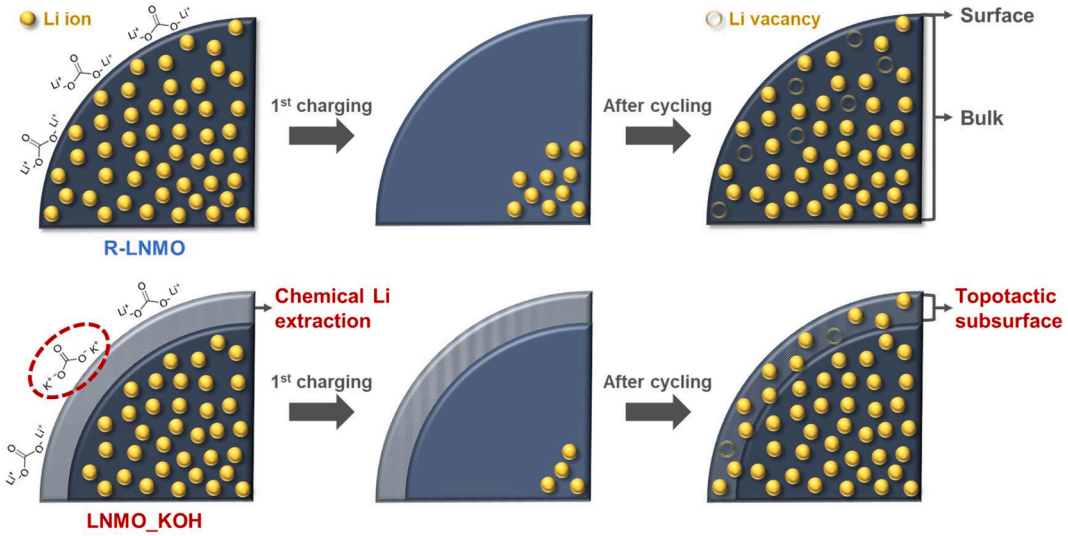

Scheme 1. Impact of a Li-vacant topotactic subsurface and K_2CO_3-enriched external surface on the Li-ion kinetics and storage properties of LNMO particles.

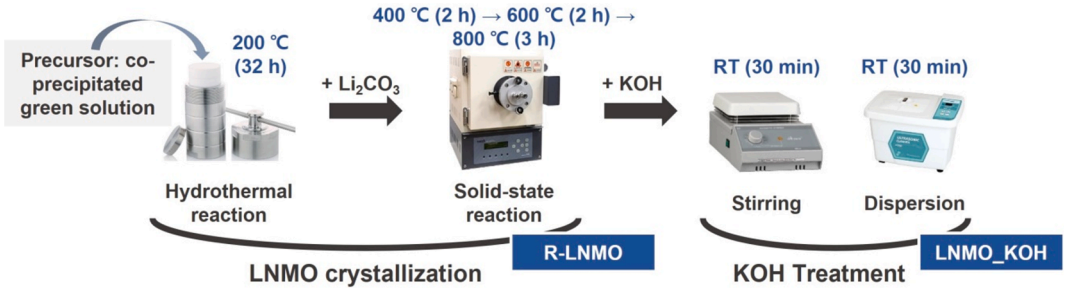

Fig. 1. Schematic representation of the synthesis processes for R-LNMO and LNMO_KOH.

under identical conditions. To further obtain the crystallographic information of the materials, Raman spectroscopy (LabRAM HR-800, Horiba) was employed. The particle morphologies of the samples were observed using field-emission scanning electron microscopy (FE-SEM; JSM-7900F,JEOL). The surface areas of R-LNMO and LNMO_KOH were estimated via Brunauer–Emmett–Teller (BET) analysis (BET; ASAP 2420, Micromeritics). Field-emission transmission electron microscopy (FE-TEM; JEM-2100F, JEOL) equipped with an electron energy loss spectroscopy (EELS; Libra 200 MC TEM, Carl Zeiss) was employed to compare the atomic arrangements in the subsurface and bulk of the LNMO_KOH particles. To determine the chemical compositions of the two samples, inductively coupled plasma-optical emission spectrometry (ICP-OES; ICP-OES 720, Agilent) was used. The chemical bond structures on the surfaces of the R-LNMO and LNMO_KOH particles were confirmed using Fourier-transform infrared spectroscopy (FT-IR; ALPHA-P, Bruker). We estimated the oxidation states of transition metals and surface chemistry before and after cycling via X-ray photoelectron spectroscopy (XPS; K-alpha$^+$, Thermo) analysis. All the collected XPS spectra were calibrated using a C–C bond with a binding energy of 284.8 eV. A thermogravimetric analysis-differential scanning calorimetry (TGA-DSC; TGA/DSC1, Mettler-Toledo) was performed up to 1000 ℃ in an N_2 atmosphere at a heating rate of 50 ℃ min^{-1}.

2.3. Electrochemical characterization

First, a slurry was prepared with a weight ratio of the active material, conductive carbon (Super-P), and polymer binder (polyvinylidene fluoride, PVDF) of 80:10:10. The slurry was pasted onto an Al foil and then dried in a vacuum oven at 120 ℃ for 12 h. The dried electrodes, with a diameter of 14 Φ, were used as the working electrodes. We adopted Li metal as the reference and counter electrodes for the 2032 coin cells. The cells were assembled in an argon-filled glove box using an electrolyte composed of 1 M $LiPF_6$ dissolved in a mixed solvent of ethylene carbonate (EC), ethyl methyl carbonate (EMC), and dimethyl carbonate (DMC) in a 1:1:1 vol ratio.

The galvanostatic charge/discharge profiles of each cell were obtained at a current density of 0.2C (where 1C = 100 mA h g^{-1}) in the voltage range between 3.5 and 4.8 V (vs. Li$^+$/Li). Electrochemical impedance spectroscopy (EIS) analysis was performed in the frequency range of 0.01 to 100 kHz, and the acquired data were processed using Zview software. Galvanostatic intermittent titration technique (GITT) profiles were obtained by repetitively charging (or discharging) at a current density of 0.1C for a pulse duration (τ) of 20 min, with a resting period of 3 h between each step. All electrochemical tests and analyses were conducted at RT.

3. Results and Discussion

Fig. 2(a) presents the XRD patterns for the R-LNMO and LNMO_KOH samples. Initially, the XRD pattern for the (Ni, Mn) carbonate precursor corresponded to the rhombohedral $MnCO_3$ phase (indexed to JCPDS Card #83–1763), with the exception of a minor peak shift (Figure S1). The substitution of Ni^{2+} ions, which have a smaller ionic radius compared to Mn^{2+} ions, reduces the overall d-spacing of the lattice planes in the $MnCO_3$ precursor, resulting in a shift of the XRD peaks to higher angles by the Bragg's law [54]. The sharp characteristic peaks observed in the diffraction patterns for R-LNMO and LNMO_KOH suggest the successful formation of crystalline LNMO materials with a spinel

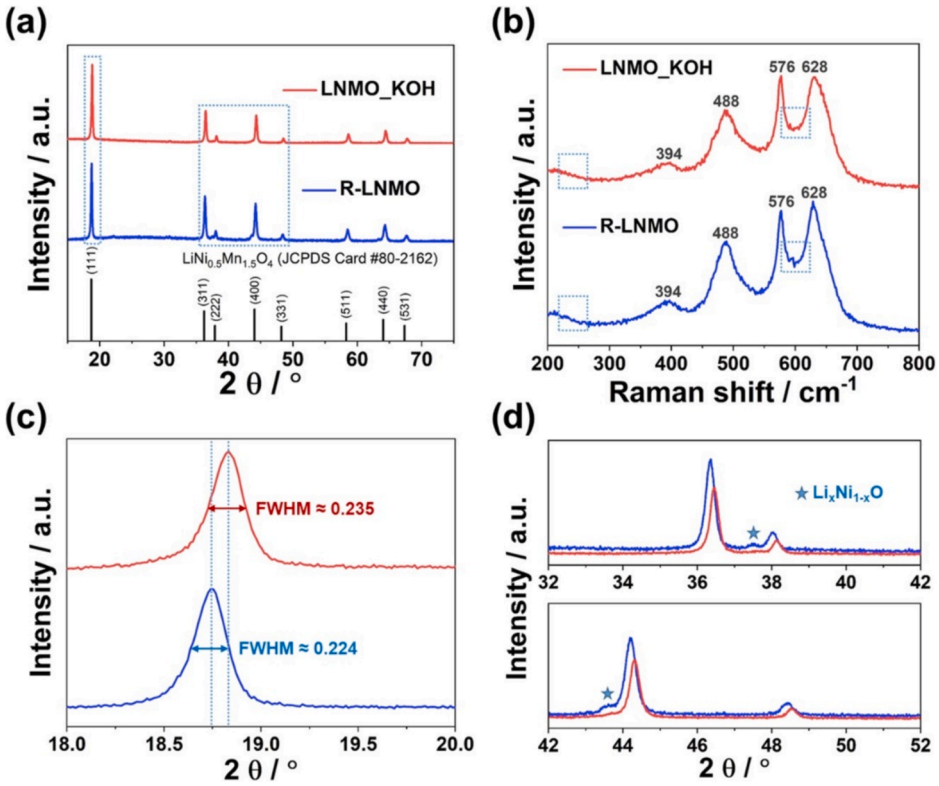

Fig. 2. (a) XRD patterns, (b) Raman spectra, (c, d) magnified XRD patterns for R-LNMO and LNMO_KOH.

structure. This is because all the experimental peaks matched those in the XRD pattern of a typical LNMO phase (indexed to JCPDS Card #80–2162). However, due to the nearly identical atomic scattering factors of Ni and Mn, it is challenging to determine whether the spinel structure of LNMO is ordered (space group: $P4_332$) or disordered (space group: Fd-3 m) through XRD analysis [55]. In contrast, Raman spectroscopy is commonly used to distinguish between these two different crystal structures. Even a subtle variation in the atomic arrangements of Ni and Mn can impact the vibration modes of cation–anion bonds in the LNMO spinel lattice [56]. Fig. 2(b) displays the Raman spectra of R-LNMO and LNMO_KOH. Consequently, both structures were identified as disordered spinel structures because an ordered spinel structure, which has lower symmetry in crystallography, would exhibit more vibration modes in the region of the Raman spectra marked in the green

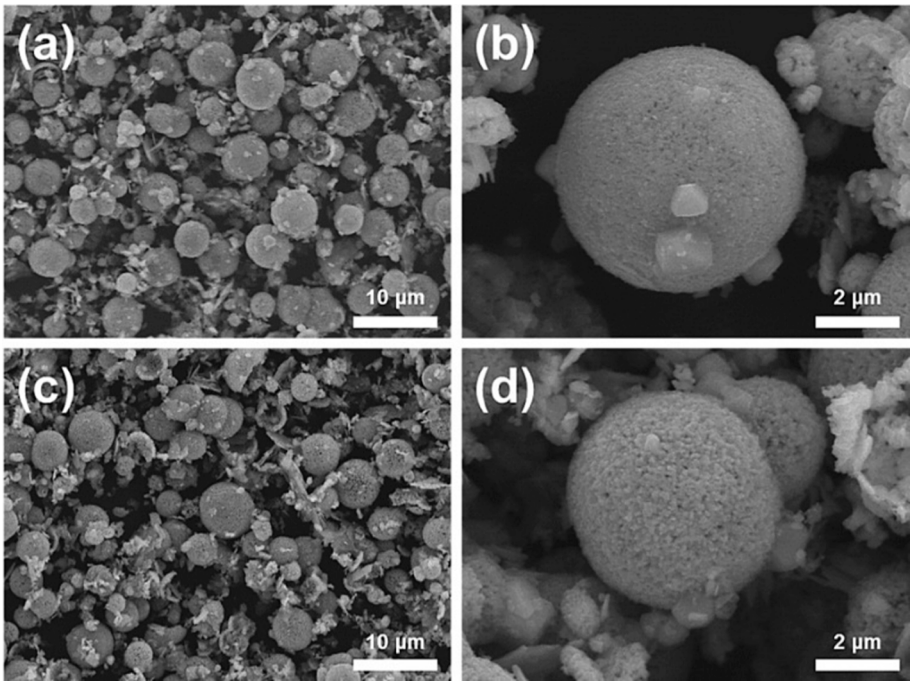

Fig. 3. Low- and high-magnification SEM images of (a, b) R-LNMO and (c, d) LNMO_KOH.

box [56,57]. However, the Raman band of LNMO_KOH observed at ~ 576 cm^{-1} (assigned to the Mn–O bond), with higher intensity compared to R-LNMO, demonstrates the oxidation of Mn induced by the KOH treatment [58,59]. Meanwhile, from the magnified (1 1 1) peaks shown in Fig. 2(c), we confirmed that the characteristic peaks for R-LNMO shifted to higher angles after the KOH treatment. At the same time, the full width at half maximum (FWHM) value, which is inversely proportional to the crystallite size according to the Scherrer equation, was larger for LNMO_KOH compared to R-LNMO. These results indicate that the average lattice parameters and crystallite size of LNMO_KOH were smaller than those of R-LNMO. Interestingly, for R-LNMO, distinctive minor peaks ($2\theta \approx 37.5°$, 43.5°) corresponding to impurity phases like $Li_xNi_{1-x}O$ were detected, but these peaks disappeared in LNMO_KOH (Fig. 2(d)).

To assess the impact of the KOH treatment on the morphology of LNMO particles, FE-SEM images of R-LNMO and LNMO_KOH are depicted in Fig. 3. For the (Ni, Mn) carbonate precursor, we observed large spherical secondary particles with dense surfaces and a diameter of ~ 5 μm (Figure S2). This specific morphology remained unchanged even after calcining the mixed precursor of (Ni, Mn) carbonate and Li_2CO_3 for the synthesis of R-LNMO (Fig. 3(a) and 3(b)). However, the surface roughness and porosity of the R-LNMO particles increased in a KOH solution (Fig. 3(c) and 3(d)), likely due to the dissolution of hydrophilic Li compounds such as LiOH. The ICP-OES analysis results for R-LNMO and LNMO_KOH, as presented in Table 1, revealed that ~ 20 % of Li^+ ions were extracted from R-LNMO after the KOH treatment. This process contributed to the reduction in the average lattice parameters, crystallite size, and impurity levels of R-LNMO (Fig. 2(c) and 2(d)). Notably, the Ni/Mn molar ratio in R-LNMO was preserved, in contrast to the Li/(Ni + Mn) ratio, indicating minimal transition metal dissolution from the R-LNMO particles into a KOH solution. This characteristic played a crucial role in preventing the collapse of the disordered spinel structure of LNMO_KOH, even in a strong basic aqueous solution, which is in agreement with the previous XRD results (Fig. 2(a)). The specific surface areas of R-LNMO and LNMO_KOH, determined via BET analysis, were confirmed to be 4.0778 and 6.2923 $m^2 g^{-1}$, respectively. Due to the increased surface area and roughness resulting from the dissolution of residual Li and chemical Li-ion extraction, the porous secondary particles of the LNMO_KOH sample could enhance electrolyte penetration and Li-ion diffusion into the smaller primary particles. Additionally, K^+ ions were presumed to be weakly bound to the extensive surface of LNMO_KOH particles rather than infiltrating into the subsurface, given that the size of K^+ ions is too large to occupy both the pre-existing tetrahedral (8a) and octahedral (16d) sites [8,16,50]. Hence, the K/(Ni + Mn) ratio was not taken into consideration when determining the chemical composition of LNMO_KOH (Table 1).

To trace the variation in atomic content (Li, K) and lattice spacing from the surface to the bulk of LNMO_KOH, we conducted FE-TEM/EELS analysis on the cross-sectional LNMO_KOH specimen prepared using a focused-ion beam (FIB) (Figure S3). As shown in Fig. 4(a), the amount of Li^+ ions abruptly decreased within the subsurface region (<0.1 μm) of LNMO_KOH. Conversely, the majority of K^+ ions were confined to the surface of LNMO_KOH particles. The Li K-edge and K L-edge EELS spectra of LNMO_KOH, observed at five different sampling points marked with each distinct color, also demonstrate such relationships (Fig. 4(b) and 4(c)) [60,61]. As mentioned in the *Introduction*, OH^- ions, which are electrostatically coupled with K^+ ions on the external surface of LNMO_KOH particles in a KOH aqueous solution, could stably extract Li^+ ions from the subsurface. As a result, the d-spacing of the (1 1 1) plane in the LNMO lattice decreased in the subsurface (~ 0.48 nm) compared to the bulk (~ 0.49 nm) (Fig. 4(d) and 4(e)). It should be noted here that the crystal structure and atomic arrangement of R-LNMO are identical to those of LNMO_KOH in the bulk because LNMO_KOH was derived from R-LNMO through the KOH surface treatment. Additionally, unlike the bulk domain corresponding to R-LNMO, a more ordered atomic arrangement, indicated by bright and dark alternating patterns, was clearly distinguishable in the subsurface of LNMO_KOH particles, resembling the TEM image of an ordered spinel LNMO reported in the latest literature [4,34]. Therefore, a topotactic transition occurred when Li^+ ions in the subsurface of the R-LNMO particles reacted with the OH^- ions adsorbed on the external surface, consistent with the results in Fig. 2(c). Furthermore, Li^+ ions could be extracted from the $Li_xNi_{1-x}O$ impurity as well as the primary LNMO phases in the subsurface of R-LNMO particles (Fig. 2(d)).

Fig. 5 displays the XPS and FT-IR spectra of R-LNMO and LNMO_KOH. First, from the O 1 s XPS spectra (Fig. 5(a) and 5(b)), LNMO_KOH showed a lower content of adsorbed H_2O molecules compared to R-LNMO. This finding coincides with the results from the FT-IR spectra of both materials depicted in Figure S4, where the characteristic peaks for H_2O (~1,630 cm^{-1}) and K_2CO_3 (~1,566 and ~ 1,447 cm^{-1}) were identified in the R-LNMO and LNMO_KOH spectra, respectively. The presence of K^+ ions on the external surface of the LNMO_KOH particles was also confirmed by the K 2p XPS spectra shown in Figure S5, which is in agreement with the ICP-OES results (Table 1). Additionally, the XPS binding energies for C–O and C = O bonds, characteristic of A_2CO_3 (A ≡ Li, K) compounds, were lower for LNMO_KOH than for R-LNMO (Fig. 5(c) and 5(d)). On the surfaces of LNMO particles for both R-LNMO and LNMO_KOH, Li_2CO_3 readily forms as a result of the chemical reactions between Li residues and CO_2 gas molecules in the vicinity of the particles. However, the binding energies between C and O atoms in the CO_3^{2-} component of A_2CO_3 could be reduced due to the weakened ionization energy-relative screening effect resulting from the replacement of Li^+ with K^+ ions following the KOH surface treatment [62]. The observed decrease in adsorbed H_2O molecules and the formation of the K_2CO_3 component on the external surfaces of R-LNMO particles can be attributed to the spontaneous chemical reaction between KOH and CO_2 (i.e., $2KOH + CO_2 \rightarrow K_2CO_3 + H_2O$) in a KOH solution [49,50].

We inferred the oxidation states of the central transition metals (Ni, Mn) in the subsurface of LNMO particles based on their Mn 3 s, Mn 2p, and Ni 2p XPS spectra. In principle, the average oxidation states of Ni and Mn in LNMO active materials are close to + 2 and + 4, respectively. However, high-temperature calcination inevitably leads to significant oxygen deficiencies, especially in the subsurface of LNMO particles, resulting in the presence of Mn^{3+} and Ni^{3+} ions within the disordered structure of R-LNMO [56]. In addition, to compensate for the chemical extraction of Li^+ ions from R-LNMO, Ni and/or Mn should oxidize, thereby maintaining the charge neutrality of LNMO_KOH even after the KOH surface treatment. As a result, Fig. 5(e) shows that the energy splitting between the two distinct peaks (ΔE_{Mn3s}) decreased from ~ 4.79 to ~ 4.65 when ~ 20 % of Li^+ ions were extracted from the subsurface of R-LNMO particles. Simultaneously, the Mn 2p XPS peak positions shifted to higher binding energy values (Figure S6). These observations imply that the Mn ions in the octahedral sites of the R-LNMO subsurface lattice were oxidized by the KOH surface treatment. Here, the average oxidation states of Mn in R-LNMO and LNMO_KOH were estimated to be ~ 3.59 and ~ 3.74, respectively, using the formula Mn oxidation state $\approx 8.95 - 1.12\Delta E_{Mn3s}$ [63,64]. By contrast, there was negligible variation in the peak positions of the Ni 2p XPS spectra of both materials (Figure S7).

Fig. 5(f) shows the FT-IR spectra of R-LNMO and LNMO_KOH observed in the range of 800–400 cm^{-1}. FT-IR analysis is highly sensitive to the vibrational behavior of cation–anion bonds, similar to Raman analysis, which varies depending on the atomic arrangements of Ni and Mn. As disorder between Ni and Mn within the spinel lattice increases,

Table 1
Results of the ICP-OES analysis for R-LNMO and LNMO_KOH.

	R-LNMO	LNMO_KOH
Li/(Ni + Mn)	0.49	0.4
Ni/Mn	2.7	2.7
K/(Ni + Mn)	–	0.009 (adsorbed)
Chemical compositions	$Li_{0.98}Ni_{0.54}Mn_{1.46}O_4$	$Li_{0.8}Ni_{0.54}Mn_{1.46}O_4$

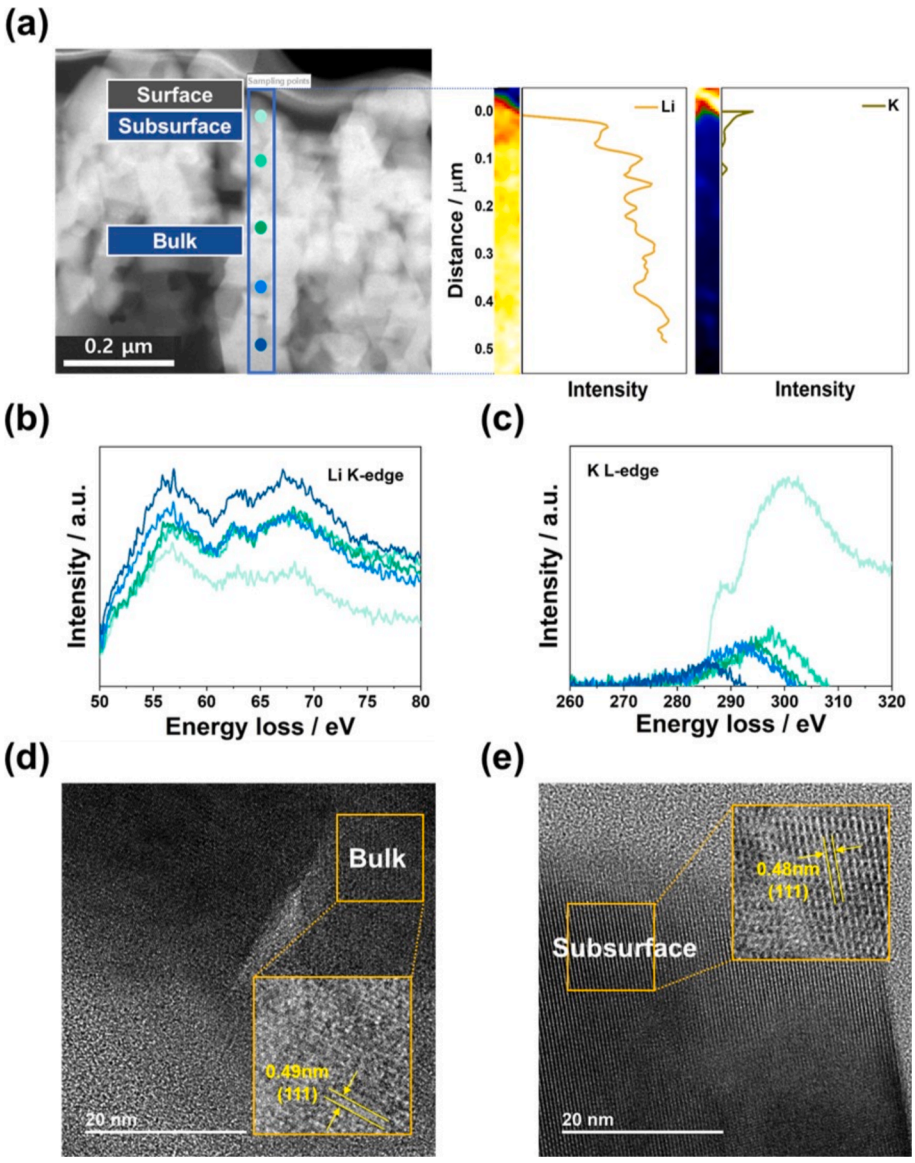

Fig. 4. (a) Mapping the atomic distribution of Li and K from the surface to the bulk of LNMO_KOH. (b) Li K-edge and (c) K L-edge EELS spectra of LNMO_KOH. FE-TEM images of LNMO_KOH obtained from (d) the bulk and (e) the subsurface.

the peak intensity ratio of Mn–O (~611 cm^{-1}) to Ni–O (~574 cm^{-1}) stretching modes increases [16,65]. Therefore, the reduced Mn–O/Ni–O peak intensity ratio in LNMO_KOH compared to R-LNMO signifies a more ordered subsurface structure in LNMO, resulting from the Li-ion extraction and subsequent Mn oxidation [21]. Specifically, the lower Mn^{3+}/Mn^{4+} atomic ratio in LNMO, induced by chemical or electrochemical delithiation, can lead to a partial phase transformation of the LNMO spinel structure from a disordered to an ordered state [34].

To interrelate the physicochemical characteristics and electrochemical performance of R-LNMO and LNMO_KOH, we first compared the galvanostatic charge/discharge cycling profiles of the materials, as shown in Fig. 6(a) and 6(b). At a current density of 0.2C (where 1C = 100 mA h/g), the charge/discharge curves of R-LNMO and LNMO_KOH exhibited almost identical configurations typical of disordered LNMO. However, the initial discharge capacities of R-LNMO and LNMO_KOH were ~ 83 and ~ 107 mA h/g, respectively. After the first cycle, these capacities gradually increased and reached their maximum values after 20 and 5 cycles for R-LNMO (~89 mA h/g) and LNMO_KOH (~110 mA h/g), respectively.

Figure S8 presents the GITT curves for R-LNMO and LNMO_KOH during the first cycle, providing quantitative insights into the Li-ion kinetics within the bulk of LNMO particles. For each pulse duration (τ) applied in the GITT tests, the open-circuit voltage (OCV) and closed-circuit voltage (CCV) values, in conjunction with their differences, can be extracted from the GITT curves as a function of the state of charge (SOC). Using these values and other physical parameters such as the actual/molar mass, molar volume, and specific surface area of the active materials, we determined the Li-ion diffusivities with respect to the SOC for both materials (Fig. 6(c)) [66]. As a result, the Li-ion diffusivity of LNMO_KOH was found to be at least 10 times higher than that of R-LNMO during the first cycle. This suggests that the Li-deficient, low-impurity, and relatively ordered subsurface environment promotes the overall migration of Li^{+} ions through the bulk of the LNMO particles. As previously discussed in Fig. 5(f), the ordered spinel phase in LNMO increases due to the oxidation of Mn^{3+} to Mn^{4+} ions [21,34], and the disordered core–ordered shell structure of LNMO improves Li-ion kinetics and structural stability during cycling by leveraging the advantages of each phase [65]. Indeed, the degree of the ordered Ni/Mn arrangement in LNMO_KOH increased concurrently with the oxidation of Mn in the subsurface of R-LNMO particles (Fig. 5(d)), which benefits

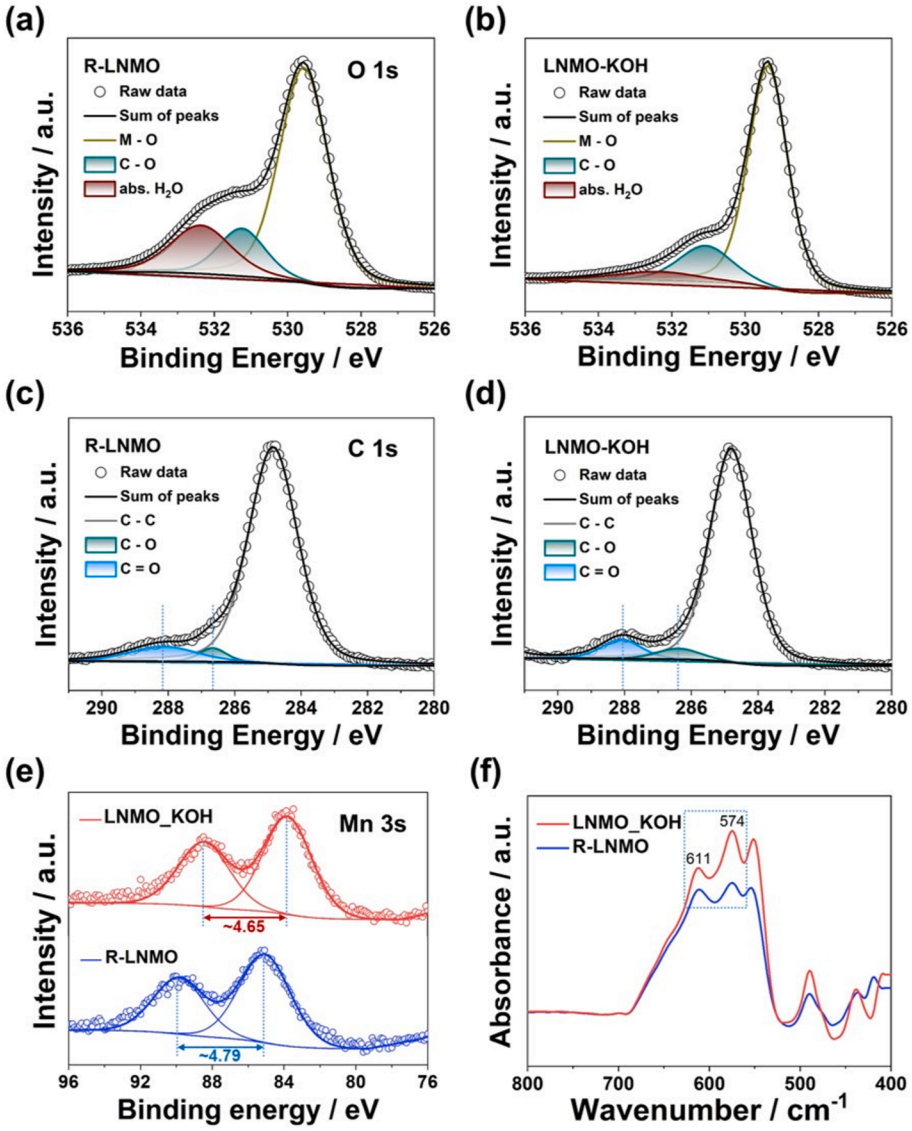

Fig. 5. XPS Spectra of (a, b) O 1 s, (c, d) C 1 s, and (e) Mn 3 s for R-LNMO and LNMO_KOH. (f) FT-IR spectra of R-LNMO and LNMO_KOH in the range of 800–400 cm^{-1}.

stable Li-ion storage and migration in LNMO_KOH.

In contrast to the GITT electrochemical method, EIS analysis is effective for evaluating the interfacial charge interactions between LNMO particles and the electrolyte. Here, we collected the EIS spectra of R-LNMO and LNMO_KOH after an initial discharge to half of their maximum practical capacity (Fig. 6(d)). These spectra reflect the effects of K_2CO_3-enriched CEI layers formed on the surfaces of LNMO particles following the oxidative decomposition of the electrolyte during the initial charge. The inset in Fig. 6(d) depicts the equivalent circuit model used to fit and interpret the spectra acquired from R-LNMO|Li and LNMO_KOH|Li half cells. The quantitative parameters derived from the Nyquist plots of EIS spectra are tabulated in Table S1, where the charge transfer resistances at the LNMO cathode/CEI and CEI/electrolyte interfaces are denoted as R_{ct}(C) and R_{CEI}, respectively. Both R_{ct}(C) and R_{CEI} were reduced as a result of the KOH surface treatment, suggesting that Li-ion transfer could be enhanced through the K_2CO_3-enriched CEI layers formed on the LNMO surfaces with a large reaction area. After 20 cycles, the differences in both R_{ct}(C) and R_{CEI} between R-LNMO and LNMO_KOH were significantly increased (Figure S9). This finding indicates that the formation of K_2CO_3-enriched CEI layers facilitates Li-ion transfer even under conditions where detrimental electrolyte decomposition occurs consistently. In addition, applications of K_2CO_3 as an electrolyte additive or coating chemical have reported that K_2CO_3 formed on the surfaces of active particles contributes to stabilizing electrode/electrolyte interfaces by reducing the contact area and inhibiting undesirable side reactions between the active particles and the electrolyte [51,52,67].

In summary, the higher reversible capacity and the fewer number of cycles required to complete cell activation for LNMO_KOH compared to R-LNMO could stem from the following significant aspects of superiority: (1) enhanced Li-ion migration through the Li-deficient, topotactic subsurface with an intensified ordered arrangement of Ni and Mn; (2) reduced detrimental impurity phases (e.g., $Li_xNi_{1-x}O$) and adsorbed H_2O molecules; (3) increased external surface area induced by chemical Li-ion extraction; and (4) chemical protection of the external surface from oxidative electrolyte decomposition in high voltage regions by partially replacing Li_2CO_3 with K_2CO_3.

Fig. 7(a) illustrates the cycling performance of R-LNMO and LNMO_KOH evaluated at a current density of 0.2C. After 100 cycles, R-LNMO and LNMO_KOH maintained ~ 91 % and ~ 97 % of their respective initial capacities. Improvements in Li-ion kinetics at both the subsurface and external surface of LNMO_KOH particles not only

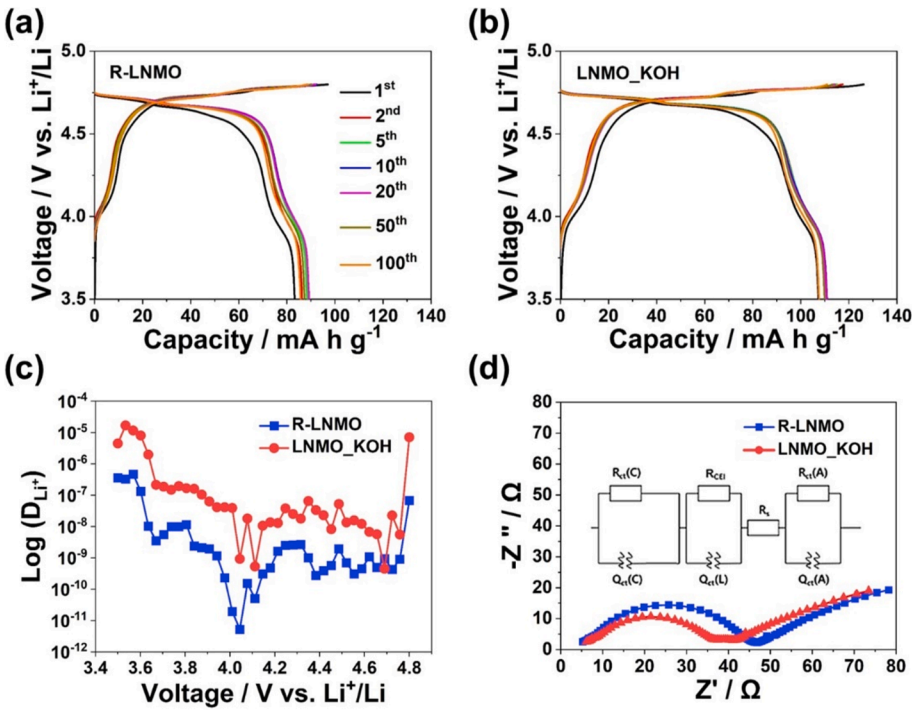

Fig. 6. Charge/discharge cycling profiles (C-rate: 0.2C) of (a) R-LNMO and (b) LNMO_KOH. (c) Li-ion diffusivity derived from the GITT curves of R-LNMO and LNMO_KOH for the first cycle. (d) EIS spectra of R-LNMO and LNMO_KOH collected at a 50% depth of discharge (DOD50).

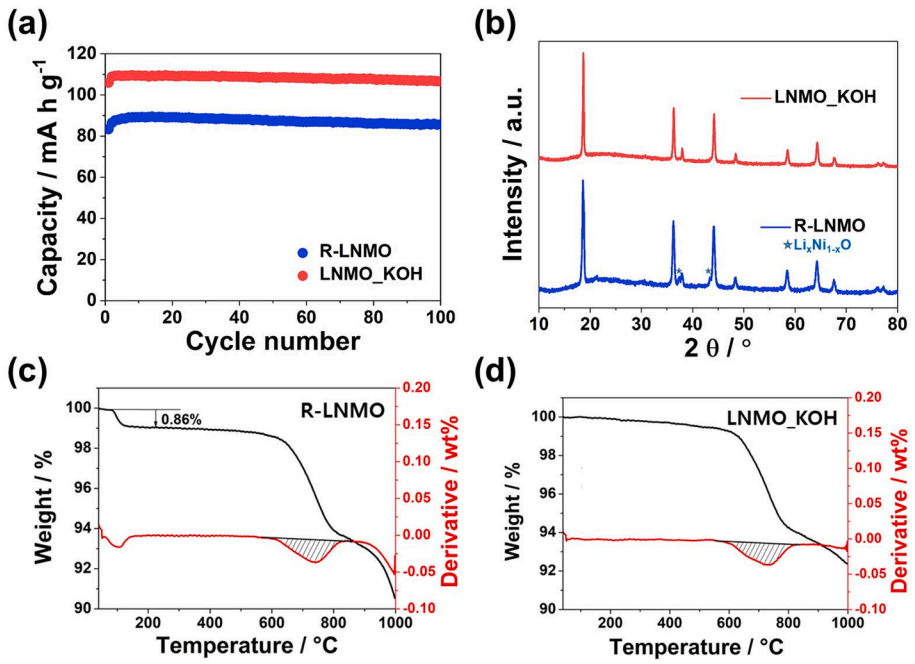

Fig. 7. (a) Cycling performance (C-rate: 0.2C) and (b) ex-situ XRD patterns (after 100 cycles) of R-LNMO and LNMO_KOH. TGA curves of (c) R-LNMO and (d) LNMO_KOH.

increased the reversible capacity but also enhanced capacity retention compared to R-LNMO. Moreover, the ex-situ XRD patterns shown in Fig. 7(b) demonstrated the outstanding structural integrity of LNMO_KOH even after 100 cycles. On the contrary, R-LNMO still exhibited the $Li_xNi_{1-x}O$ impurity phase, observed at $2\theta \approx 37.5°$, 43.5°, with a rock-salt structure that hinders Li-ion transport into/out of the LNMO primary phase during cycling [18,32]. Surprisingly, ex-situ Raman analysis revealed that the degree of the ordered Ni/Mn arrangement in LNMO_KOH was enhanced with cycling (Figure S10). Considering the benefits of ordered spinel LNMO with superior structural stability [18,21], further studies are imperative to verify the undisclosed mechanism of the phase transition toward a more ordered spinel character of LNMO with a Li-vacant topotactic subsurface.

Fig. 7(c) and 7(d) display TGA curves of R-LNMO and LNMO_KOH. The observed weight loss (0.86 %) of R-LNMO at ~ 100 ℃ (i.e., the boiling point of H_2O) suggests inherent susceptibility of LNMO particle

surfaces to humidity, as supported by previous XPS and FT-IR analyses (Fig. 5(a) and S4). In contrast, the presence of K_2CO_3 components formed on the LNMO surfaces appeared to prevent the adsorption of H_2O molecules (Fig. 7(d)). Given that even trace amounts of H_2O in organic electrolytes can generate HF, which accelerates the dissolution of transition metals from the LNMO particles into the electrolyte [68,69], the absence of adsorbed H_2O molecules likely contributed to the excellent cycling performance of LNMO_KOH. At elevated temperatures between 600 ℃ and 800 ℃, both LNMO materials showed similar weight loss due to thermal decomposition induced by oxygen evolution from the spinel lattices [70]. Although LNMO_KOH was prepared by chemically extracting ~ 20 % of Li^+ ions from R-LNMO, it demonstrated enhanced thermal stability compared to R-LNMO, even at temperatures exceeding 800 ℃, where an irreversible phase transition from spinel to cation-deficient rock-salt structure occurs. This is important because the chemical reactivity of LNMO at the CEI layers generally increases with SOC or the degree of delithiation, potentially compromising the structural stability of LNMO at high temperatures [8]. The superior structural integrity of LNMO_KOH is associated with a high proportion of a thermally stable, ordered Ni/Mn arrangement in its subsurface, while effectively minimizing the presence of unstable impurity phases therein. Consequently, KOH-assisted chemical delithiation technology is expected to promote improvements in the electrochemical performance and thermal stability of LNMO cathode materials.

4. Conclusion

In conclusion, we have successfully developed $LiNi_{0.5}Mn_{1.5}O_4$ (LNMO) cathode materials with enhanced Li-ion kinetics and storage properties through a KOH-assisted wet chemistry method. The resulting surface-modified LNMO (LNMO_KOH) exhibits a Li-vacant topotactic subsurface and a K_2CO_3-enriched external surface. Both the referenced LNMO (R-LNMO) and LNMO_KOH were confirmed to possess disordered spinel structures, as demonstrated by the results of the Raman analysis. Notably, the KOH treatment led to a decrease in the average lattice parameters, crystallite size, and impurity levels of R-LNMO, indicating the effective chemical extraction of Li^+ ions from the subsurface. While the ICP-OES analysis revealed that ~ 20 % of Li ions were extracted from R-LNMO, the Ni/Mn molar ratio in R-LNMO remained unchanged after the KOH treatment. In contrast to Ni, the oxidation of Mn due to the Li-ion extraction enhanced the ordered atomic arrangement of Ni and Mn in the subsurface of LNMO_KOH particles. These findings were corroborated by the FE-TEM/EELS and XPS analyses. Additionally, the KOH treatment facilitated the removal of adsorbed H_2O molecules and the formation of K_2CO_3 on the external surfaces of R-LNMO particles through a chemical reaction between KOH and CO_2 (i.e., $2KOH + CO_2 \rightarrow K_2CO_3 + H_2O$). Improvements in the charge/discharge cycling performance and thermal stability of LNMO were also observed following the KOH surface treatment. Remarkably, LNMO_KOH exhibited superior electrochemical performance, achieving a high discharge capacity of ~ 110 mA h/g and an impressive capacity retention of ~ 97 % after 100 cycles at 0.2C. By contrast, R-LNMO delivered a discharge capacity of ~ 89 mA h/g and a capacity retention of ~ 91 % under the same cycle number and current density. These enhancements can be attributed to improved Li-ion migration facilitated by the Li-deficient, topotactic subsurface with an intensified ordered Ni/Mn arrangement, reduced levels of detrimental impurity phases and adsorbed H_2O molecules, as well as K_2CO_3-assisted chemical protection of the external surface of LNMO particles. Therefore, this study establishes a foundation for the development of novel high-voltage cathode materials by optimizing the subsurface and external surface properties of active particles, which contributes to improvements in their charge storage capacity and Li-ion kinetics.

CRediT authorship contribution statement

Taekyun Jeong: Writing – original draft, Methodology, Conceptualization. **Sungkyoung Kang:** Formal analysis. **Seonguk Lim:** Software, Investigation. **Sieun An:** Visualization. **Chungsun Oh:** Validation. **Jun-Ho Park:** Resources, Funding acquisition, Data curation. **Dongwook Han:** Writing – review & editing, Supervision, Project administration.

Declaration of competing interest

The authors declare that they have no known competing financial interests or personal relationships that could have appeared to influence the work reported in this paper.

Acknowledgment

This study was financially supported by Seoul National University of Science and Technology (2024-0767) and also supported by the Nano & Material Technology Development Program through the National Research Foundation of Korea(NRF) funded by Ministry of Science and ICT(RS-2024-00408823, Developement of single crystal cathode synthesis for spent battery upcycling based on sliding-door type cell dismantling and inter-particle equilibrium of lithium composition).

Appendix A. Supplementary data

Supplementary data to this article can be found online at https://doi.org/10.1016/j.cej.2024.156590.

Data availability

Data will be made available on request.

References

[1] R. Schmuch, R. Wagner, G. Hörpel, T. Placke, M. Winter, Performance and cost of materials for lithium-based rechargeable automotive batteries, Nat. Energy 3 (2018) 267–278, https://doi.org/10.1038/s41560-018-0107-2.
[2] J.B. Goodenough, K.-S. Park, The Li-ion rechargeable battery: A perspective, J. Am. Chem. Soc. 135 (2013) 1167–1176, https://doi.org/10.1021/ja3091438.
[3] W. Li, E.M. Erickson, A. Manthiram, High-nickel layered oxide cathodes for lithium-based automotive batteries, Nat. Energy 5 (2020) 26–34, https://doi.org/10.1038/s41560-019-0513-0.
[4] X. Zhu, A. Huang, I. Martens, N. Vostrov, Y. Sun, M.-I. Richard, T.U. Schülli, L. Wang, High-Voltage Spinel Cathode Materials: Navigating the Structural Evolution for Lithium-Ion Batteries, Adv. Mater. 36 (2024) 2403482, https://doi.org/10.1002/adma.202403482.
[5] S.S. Zhang, Problems and their origins of Ni-rich layered oxide cathode materials, Energy Storage Mater. 24 (2020) 247–254, https://doi.org/10.1016/j.ensm.2019.08.013.
[6] X. Kong, Y. Zhang, J. Li, H. Yang, P. Dai, J. Zeng, J. Zhao, Single-crystal structure helps enhance the thermal performance of Ni-rich layered cathode materials for lithium-ion batteries, Chem. Eng. J. 434 (2022) 134638, https://doi.org/10.1016/j.cej.2022.134638.
[7] Y. Wang, Q. Zhang, Z.-C. Xue, L. Yang, J. Wang, F. Meng, Q. Li, H. Pan, J.-N. Zhang, Z. Jiang, W. Yang, X. Yu, L. Gu, H. Li, An In Situ Formed Surface Coating Layer Enabling $LiCoO_2$ with Stable 4.6 V High-Voltage Cycle Performances, Adv. Energy Mater. 10 (2020) 2001413, https://doi.org/10.1002/aenm.202001413.
[8] X. Yu, W.A. Yu, A. Manthiram, Advances and Prospects of High-Voltage Spinel Cathodes for Lithium-Based Batteries, Small Methods 5 (2021) 2001196, https://doi.org/10.1002/smtd.202001196.
[9] G. Liang, V.K. Peterson, K.W. See, Z. Guo, W.K. Pang, Developing high-voltage spinel $LiNi_{0.5}Mn_{1.5}O_4$ cathodes for high-energy-density lithium-ion batteries: Current achievements and future prospects, J. Mater. Chem. A 8 (2020) 15373–15398, https://doi.org/10.1039/D0TA02812F.
[10] J. Xiang, Y. Wei, Y. Zhong, Y. Yang, H. Cheng, L. Yuan, H. Xu, Y. Huang, Building Practical High-Voltage Cathode Materials for Lithium-Ion Batteries, Adv. Mater. 34 (2022) 2200912, https://doi.org/10.1002/adma.202200912.
[11] J. Chen, Z. Huang, W. Zeng, F. Cao, J. Ma, W. Tian, S. Mu, Synthesis, Modification, and Lithium-Storage Properties of Spinel $LiNi_{0.5}Mn_{1.5}O_4$, ChemElectroChem 8 (2021) 608–624, https://doi.org/10.1002/celc.202001414.
[12] D. Li, W. Zhang, K. Chang, Y. Yuan, H.J. Seifert, Thermodynamic/Electrochemical Description of High-Voltage Spinels for Lithium-Ion Batteries, J. Electrochem. Soc. 167 (2020) 130511. https://iopscience.iop.org/article/10.1149/1945-7111/abb7ec.

[13] F. Kong, G. Zhang, D. Wu, F. Sun, S. Tao, S. Chu, B. Qian, W. Chu, L. Song, Insight into the cation migration and surface structural evolution of spinel $LiNi_{0.5}Mn_{1.5}O_4$ cathode material for lithium-ion batteries, Chem. Eng. J. 451 (2023) 138708, https://doi.org/10.1016/j.cej.2022.138708.

[14] X. Hou, X. Liu, H. Wang, X. Zhang, J. Zhou, M. Wang, Specific countermeasures to intrinsic capacity decline issues and future direction of $LiMn_2O_4$ cathode, Energy Storage Mater. 57 (2023) 577–606, https://doi.org/10.1016/j.ensm.2023.02.015.

[15] Z.I. Radzi, K.H. Arifin, M.Z. Kufian, V. Balakrishnan, S.R.S. Raihan, N.A. Rahim, R. Subramaniam, Review of spinel $LiMn_2O_4$ cathode materials under high cut-off voltage in lithium-ion batteries: Challenges and strategies, J. Electroanal. Chem. 920 (2022) 116623, https://doi.org/10.1016/j.jelechem.2022.116623.

[16] T.-F. Yi, J. Mei, Y.-R. Zhu, Key strategies for enhancing the cycling stability and rate capacity of $LiNi_{0.5}Mn_{1.5}O_4$ as high-voltage cathode materials for high power lithium-ion batteries, J. Power Sources 316 (2016) 85–105, https://doi.org/10.1016/j.jpowsour.2016.03.070.

[17] M. Okada, Y.-S. Lee, M. Yoshio, Cycle characterizations of $LiM_xMn_{2-x}O_4$ (M=Co, Ni) materials for lithium secondary battery at wide voltage region, J. Power Sources 90 (2000) 196–200, https://doi.org/10.1016/S0378-7753(00)00410-9.

[18] R. Amin, N. Muralidharan, R.K. Petla, H.B. Yahia, S.A.J. Al-Hail, R. Essehli, C. Daniel, M.A. Khaleel, I. Belharouak, Research advances on cobalt-free cathodes for Li-ion batteries - The high voltage $LiMn_{1.5}Ni_{0.5}O_4$ as an example, J. Power Sources 167 (2020) 228318, https://doi.org/10.1016/j.jpowsour.2020.228318.

[19] N. Piao, P.-F. Wang, L. Chen, T. Deng, X. Fan, L. Wang, X. He, Nonflammable all-fluorinated electrolytes enabling high-power and long-life $LiNi_{0.5}Mn_{1.5}O_4$/$Li_4Ti_5O_{12}$ lithium-ion batteries, Nano Energy 105 (2023) 108040, https://doi.org/10.1016/j.nanoen.2022.108040.

[20] N. Arun, V. Aravindan, S. Jayaraman, S. Madhavi, Unveiling the Fabrication of "Rocking-Chair" Type 3.2 and 1.2 V Class Cells Using Spinel $LiNi_{0.5}Mn_{1.5}O_4$ as Cathode with $Li_4Ti_5O_{12}$, J. Phys. Chem. C 119 (2015) 24332–24336. https://doi.org/10.1021/acs.jpcc.5b09290.

[21] H. Sun, A. Hu, S. Spence, C. Kuai, D. Hou, L. Mu, J. Liu, L. Li, C. Sun, S. Sainio, D. Nordlund, W. Luo, Y. Huang, F. Lin, Tailoring Disordered/Ordered Phases to Revisit the Degradation Mechanism of High-Voltage $LiNi_{0.5}Mn_{1.5}O_4$ Spinel Cathode Materials, Adv. Funct. Mater. 32 (2022) 2112279, https://doi.org/10.1002/adfm.202112279.

[22] M. Xu, M. Yang, M. Chen, L. Gu, L. Luo, S. Chen, J. Chen, B. Liu, X. Han, Enabling structural and interfacial stability of 5 V spinel $LiNi_{0.5}Mn_{1.5}O_4$ cathode by a coherent interface, J. Energy Chem. 76 (2023) 266–276, https://doi.org/10.1016/j.jechem.2022.09.021.

[23] Z. Lian, B. Zhang, Y. Zhang, X. Yu, Z. Wang, Y. Huang, J. Duan, D. Wang, X. Zeng, P. Dong, Y. Zhang, Improving electrochemical performance of $LiNi_{0.5}Mn_{1.5}O_4$ positive electrodes via regulated cathode electrolyte interphase, Chem. Eng. J. Adv. 16 (2023) 100524, https://doi.org/10.1016/j.ceja.2023.100524.

[24] D. Guan, J. Zeng, Z. Xue, Y. Cao, G. Hu, Z. Peng, K. Du, Rational Design of the Li^+-Solvation Structure Contributes to Constructing a Robust Cathode-Electrolyte Interphase for a 5 V High-Voltage $LiNi_{0.5}Mn_{1.5}O_4$ Cathode, ACS Appl, Energy Mater. 6 (2023) 9568–9576, https://doi.org/10.1021/acsaem.3c01592.

[25] B. Aktekin, M.J. Lacey, T. Nordh, R. Younesi, C. Tengstedt, W. Zipprich, D. Brandell, K. Edström, Understanding the Capacity Loss in $LiNi_{0.5}Mn_{1.5}O_4$–$Li_4Ti_5O_{12}$ Lithium-Ion Cells at Ambient and Elevated Temperatures, J. Phys. Chem. C 122 (2018) 11234–11248. https://doi.org/10.1021/acs.jpcc.8b02204.

[26] Y. Luo, Z. Cui, C. Wu, B. Sa, C. Wen, H. Li, J. Huang, C. Xu, Z. Xu, Enhanced Electrochemical Performance of a Ti–Cr-Doped $LiMn_{1.5}Ni_{0.5}O_4$ Cathode Material for Lithium-Ion Batteries, ACS Omega 8 (2023) 22721–22731, https://doi.org/10.1021/acsomega.3c01524.

[27] N.N. Intan, K. Klyukin, V. Alexandrov, Ab Initio Modeling of Transition Metal Dissolution from the $LiNi_{0.5}Mn_{1.5}O_4$ Cathode, ACS Appl, Mater. Interfaces 11 (2019) 20110–20116, https://doi.org/10.1021/acsami.9b06010.

[28] S. Zheng, Y. Yi, F. Hai, X. Gao, X. Tian, Z. Wu, J. Guo, W. Tang, W. Hua, L. Qu, M. Li, Synthesis of high-voltage spinel $LiNi_{0.5}Mn_{1.5}O_4$ by Mn_2O_3 nanosheets for lithium-ion batteries with superior cycle life span, J Energy Storage 90 (2024) 111895, https://doi.org/10.1016/j.est.2024.111895.

[29] M. Xu, B. Sheng, Y. Cheng, J. Lu, M. Chen, P. Wang, B. Liu, J. Chen, X. Han, M.-S. Wang, S. Shi, One-step calcination synthesis of interface-coherent crystallized and surface-passivated $LiNi_{0.5}Mn_{1.5}O_4$ for high-voltage lithium-ion battery, Nano Res. 17 (2024) 4192–4202, https://doi.org/10.1007/s12274-023-6361-z.

[30] J. Zeng, K. Wu, N. Li, L. He, B. Wang, X. Lin, E. Zhao, Revisiting the Temperature-Dependent Phase Structure of Spinel $LiNi_{0.5}Mn_{1.5}O_4$ for Lithium-Ion Batteries, ACS Appl. Energy Mater. 7 (2024) 2405–2415, https://doi.org/10.1021/acsaem.3c03204.

[31] C.-P. Shih, M. Krajewski, P. Hasin, C.-H. Chen, C.-Y. Lee, J.-Y. Lin, Spray-drying synthesis of fluorine-doped $LiNi_{0.5}Mn_{1.5}O_4$ as high-voltage cathodes for lithium-ion batteries, J. Alloys Compd. 932 (2023) 167641, https://doi.org/10.1016/j.jallcom.2022.167641.

[32] P. Stüble, V. Mereacre, H. Geßwein, J.R. Binder, On the Composition of $LiNi_{0.5}Mn_{1.5}O_4$ Cathode Active Materials, Adv. Energy Mater. 13 (2023) 2203778, https://doi.org/10.1002/aenm.202203778.

[33] W. Li, X. Wang, D. Wu, D. Kong, H. Wu, L. Mang, B. Liao, O. Tegus, Y. Cao, O. Haschuluu, Study on high voltage (5 V) spinel lithium manganese oxide $LiNi_{0.5}Mn_{1.5}O_4$ by doping niobium, Micro, Nano Lett. 19 (2024) e12192.

[34] B. Aktekin, F. Massel, M. Ahmadi, M. Valvo, M. Hahlin, W. Zipprich, F. Marzano, L. Duda, R. Younesi, K. Edström, D. Brandell, How Mn/Ni Ordering Controls Electrochemical Performance in High-Voltage Spinel $LiNi_{0.44}Mn_{1.56}O_4$ with Fixed Oxygen Content, ACS Appl, Energy Mater. 3 (2020) 6001–6013, https://doi.org/10.1021/acsaem.0c01075.

[35] P. Hou, Z. Lin, F. Li, X. Xu, General Synthesis of Single-Crystal Spinel Cathodes with the Tailored Orientation of Exposed Crystal Planes for Advanced Lithium-Ion Batteries, Small 19 (2023) 2304482, https://doi.org/10.1002/smll.202304482.

[36] C. Gao, H. Liu, S. Bi, H. Li, C. Ma, Investigation the improvement of high voltage spinel $LiNi_{0.5}Mn_{1.5}O_4$ cathode material by anneal process for lithium ion batteries, Green, Energy Environ. 6 (2021) 114–123, https://doi.org/10.1016/j.gee.2020.03.001.

[37] J. Mu, X. Li, R. He, L. Sun, X. Bai, L. Zhang, P. Liu, Z. Liu, J. Gao, A. Wei, Effect of lithium-containing inorganic phosphate additives in stabilization of carbonate-based electrolyte for 5 V $LiNi_{0.5}Mn_{1.5}O_4$-based lithium-ion batteries, J Energy Storage 96 (2024) 112538, https://doi.org/10.1016/j.est.2024.112538.

[38] M.T. Nguyen, H.Q. Pham, J.A. Berrocal, I. Gunkel, U. Steiner, An electrolyte additive for the improved high voltage performance of $LiNi_{0.5}Mn_{1.5}O_4$ (LNMO) cathodes in Li-ion batteries, J. Mater. Chem. A 11 (2023) 7670–7678, https://doi.org/10.1039/D2TA09930F.

[39] Z.A. Qureshi, H.A. Tariq, R.A. Shakoor, R. Kahraman, S. AlQaradawi, Impact of coatings on the electrochemical performance of $LiNi_{0.5}Mn_{1.5}O_4$ cathode materials: A focused review, Ceram. Int. 48 (2022) 7374–7392, https://doi.org/10.1016/j.ceramint.2021.12.118.

[40] U. Nisar, J. Bansmann, M. Hebel, B. Reichel, M. Mancini, M. Wohlfahrt-Mehrens, M. Hölzle, P. Axmann, Borate modified Co-free $LiNi_{0.5}Mn_{1.5}O_4$ cathode material: A pathway to superior interface and cycling stability in LNMO/graphite full-cells, Chem. Eng. J. 493 (2024) 152416, https://doi.org/10.1016/j.cej.2024.152416.

[41] Q. Wang, L. Liu, H. Li, G. Yang, A.N. Alodhayb, J. Ma, Recent advance in coating strategies for lithium-rich manganese-based cathode materials, J. Mater. Sci. Technol. 207 (2025) 274–294, https://doi.org/10.1016/j.jmst.2024.02.094.

[42] Y. Su, J. Zhao, J. Dong, Q. Shi, J. Hao, W. Li, L. Bao, Y. Lu, N. Li, D. Cao, L. Chen, F. Wu, Atomic pins bridging integrated surface to assist high-rate stability for Co-free Li-rich cathode, Chem Eng. J. 475 (2023) 145991, https://doi.org/10.1016/j.cej.2023.145991.

[43] R.A. Zulkipli, I. Perdana1, D.R. Aprilianto, T. Rahmawati, Selective Extraction of Lithium from Spent-NMC Battery Cathodes Using Sodium Hydroxide as a Leaching Agent at Elevated Temperatures, Recent Innov. Chem. Eng. 17 (2024) 156–168. https://www.eurekaselect.com/article/139048.

[44] S.A. Chang, A. Balouch, Abdullah, Analytical perspective of lithium extraction from brine waste: Analysis and current progress, Microchem. J. 200 (2024) 110291, https://doi.org/10.1016/j.microc.2024.110291.

[45] J. Zhang, Y. Lei, Z. Lin, P. Xie, H. Lu, J. Xu, A novel approach to recovery of lithium element and production of holey graphene based on the lithiated graphite of spent lithium ion batteries, Chem. Eng. J. 436 (2022) 135011, https://doi.org/10.1016/j.cej.2022.135011.

[46] R. Pulido, N. Naveas, R.J. Martín-Palma, T. Graber, I. Brito, J. Hernández-Montelongo, M.M. Silván, Experimental and density functional theory study of the Li^+ desorption in spinel/layered lithium manganese oxide nanocomposites using HCl, Chem. Eng. J. 441 (2022) 136019, https://doi.org/10.1016/j.cej.2022.136019.

[47] C.P. Lawagon, G.M. Nisola, R.A.I. Cuevas, H. Kim, S.-P. Lee, W.-J. Chung, $Li_{1-x}Ni_{0.33}Co_{1/3}Mn_{1/3}O_2$/Ag for electrochemical lithium recovery from brine, Chem. Eng. J. 348 (2018) 1000–1011, https://doi.org/10.1016/j.cej.2018.05.030.

[48] S.-Q. Lu, Q. Zhang, F. Meng, Y.-N. Liu, J. Mao, S. Guo, M.-Y. Qi, Y.-S. Xu, Y. Qiao, S.-D. Zhang, K. Jiang, L. Gu, Y. Xia, S. Chen, G. Chen, A.-M. Cao, L.-J. Wan, Surface Lattice Modulation through Chemical Delithiation toward a Stable Nickel-Rich Layered Oxide Cathode, J. Am. Chem. Soc. 145 (2023) 7397–7407, https://doi.org/10.1021/jacs.2c13787.

[49] S. Gorthy, S. Verma, N. Sinha, S. Shetty, H. Nguyen, M. Neurock, Theoretical Insights into the Effects of KOH Concentration and the Role of OH^- in the Electrocatalytic Reduction of CO_2 on Au, ACS Catal. 13 (2023) 12924–12940, https://doi.org/10.1021/acscatal.2c06115.

[50] H.E. King, A. Salisbury, J. Huijsmans, N.Y. Dzade, O. Plümper, Influence of Inorganic Solution Components on Lithium Carbonate Crystal Growth, Cryst. Growth Des. 19 (2019) 6994–7006, https://doi.org/10.1021/acs.cgd.9b00782.

[51] Q.-C. Zhuang, J. Li, L.-L. Tian, Potassium carbonate as film forming electrolyte additive for lithium-ion batteries, J. Power Sources 15 (2013) 177–183, https://doi.org/10.1016/j.jpowsour.2012.08.050.

[52] S.M. Wood, C.H. Pham, R. Rodriguez, S.S. Nathan, A.D. Dolocan, H. Celio, J.P. de Souza, K.C. Klavetter, A. Heller, C.B. Mullins, K^+ Reduces Lithium Dendrite Growth by Forming a Thin, Less-Resistive Solid Electrolyte Interphase, ACS Energy Lett. 1 (2016) 414–419, https://doi.org/10.1021/acsenergylett.6b00259.

[53] Y. Xue, Z. Wang, F. Yu, Y. Zhang, G. Yin, Ethanol-assisted hydrothermal synthesis of $LiNi_{0.5}Mn_{1.5}O_4$ with excellent long-term cyclability at high rate for lithium-ion batteries, J. Mater. Chem. A 2 (2014) 4185–4191, https://doi.org/10.1039/C3TA14567K.

[54] Q. Li, Z. Liu, C. Wang, Y. Zhao, R. Che, Doping of Ni and Zn Elements in $MnCO_3$: High-Power Anode Material for Lithium-Ion Batteries, Small 14 (2018) 1702574, https://doi.org/10.1002/smll.201702574.

[55] J.-H. Kim, S.-T. Myung, C.S. Yoon, S.G. Kang, Y.-K. Sun, Comparative Study of $LiNi_{0.5}Mn_{1.5}O_{4-\delta}$ and $LiNi_{0.5}Mn_{1.5}O_4$ Cathodes Having Two Crystallographic Structures: $Fd\bar{3}m$ and $P4_332$, Chem. Mater. 16 (2004) 906–914, https://doi.org/10.1021/cm035050s.

[56] J. Song, D.W. Shin, Y. Lu, C.D. Amos, A. Manthiram, J.B. Goodenough, Role of Oxygen Vacancies on the Performance of $Li[Ni_{0.5-x}Mn_{1.5+x}]O_4$ (x = 0, 0.05, and 0.08) Spinel Cathodes for Lithium-Ion Batteries, Chem. Mater. 24 (2012) 3101–3109, https://doi.org/10.1021/cm301825h.

[57] C.M. Julien, F. Gendron, A. Amdouni, M. Massot, Lattice vibrations of materials for lithium rechargeable batteries. VI: Ordered spinels, Mater. Sci. Eng. b. 130 (2006) 41–48, https://doi.org/10.1016/j.mseb.2006.02.003.

[58] D. Aurbach, B. Markovsky, Y. Talyossef, G. Salitra, H.-J. Kim, S. Choi, Studies of cycling behavior, ageing, and interfacial reactions of $LiNi_{0.5}Mn_{1.5}O_4$ and carbon electrodes for lithium-ion 5-V cells, J. Power Sources 162 (2006) 780–789, https://doi.org/10.1016/j.jpowsour.2005.07.009.

[59] P. Jehnichen, C. Korte, Operando Raman Spectroscopy Measurements of a High-Voltage Cathode Material for Lithium-Ion Batteries, Anal. Chem. 91 (2019) 8054–8061, https://doi.org/10.1021/acs.analchem.8b05819.

[60] N. Taguchi, M. Kitta, H. Sakaebe, M. Kohyama, T. Akita, Lithium analysis using reflection EELS for lithium compounds, J. Electron. Spectrosc. Relat. Phenom. 203 (2015) 40–44, https://doi.org/10.1016/j.elspec.2015.05.014.

[61] L. Guan, K. Suenaga, Z. Shi, Z. Gu, S. Iijima, Direct Imaging of the Alkali Metal Site in K-Doped Fullerene Peapods, Phys. Rev. Lett. 94 (2005) 045502, https://doi.org/10.1103/PhysRevLett.94.045502.

[62] L. Caracciolo, L. Madec, H. Martinez, XPS Analysis of K-based Reference Compounds to Allow Reliable Studies of Solid Electrolyte Interphase in K-ion Batteries, ACS Appl. Energy Mater. 4 (2021) 11693–11699, https://doi.org/10.1021/acsaem.1c02400.

[63] W. Chen, G. Li, A. Pei, Y. Li, L. Liao, H. Wang, J. Wan, Z. Liang, G. Chen, H. Zhang, J. Wang, Y. Cui, A manganese–hydrogen battery with potential for grid-scale energy storage, Nat. Energy 3 (2018) 428–435, https://doi.org/10.1038/s41560-018-0147-7.

[64] D. Wang, L. Wang, G. Liang, H. Li, Z. Liu, Z. Tang, J. Liang, C. Zhi, A Superior δ-MnO_2 Cathode and a Self-Healing Zn-δ-MnO_2 Battery, ACS Nano 13 (2019) 10643–10652, https://doi.org/10.1021/acsnano.9b04916.

[65] F. Lian, F. Zhang, L. Yang, L. Ma, Y. Li, Constructing a Heterostructural $LiNi_{0.4}Mn_{1.6}O_{4-\delta}$ Material from Concentration-Gradient Framework to Significantly Improve Its Cycling Performance, ACS Appl, Mater. Interfaces 9 (2017) 15822–15829, https://doi.org/10.1021/acsami.7b01235.

[66] Z. Li, F. Du, X. Bie, D. Zhang, Y. Cai, X. Cui, C. Wang, G. Chen, Y. Wei, Electrochemical Kinetics of the $Li[Li_{0.23}Co_{0.3}Mn_{0.47}]O_2$ Cathode Material Studied by GITT and EIS, J. Phys. Chem. C 114 (2010) 22751–22757. https://doi.org/10.1021/jp1088788.

[67] S. Komaba, M. Watanabe, H. Groult, N. Kumagai, Alkali carbonate-coated graphite electrode for lithium-ion batteries, Carbon 46 (2008) 1184–1193, https://doi.org/10.1016/j.carbon.2008.04.021.

[68] K. Wang, A.J.K. Tieu, Z. Wei, Y. Zhou, L. Zhang, S. Li, K. Zeng, F. Shen, S. Adams, X. Han, Stabilizing $LiNi_{0.8}Co_{0.1}Mn_{0.1}O_2$ cathode by combined moisture and HF digestion/adsorption for high-performance lithium metal batteries, Energy Storage Mater. 67 (2024) 103275, https://doi.org/10.1016/j.ensm.2024.103275.

[69] Y. Tesfamhret, H. Liu, Z. Chai, E. Berg, R. Younesi, On the Manganese Dissolution Process from $LiMn_2O_4$ Cathode Materials, ChemElectroChem 8 (2021) 1516–1523, https://doi.org/10.1002/celc.202001496.

[70] D. Pasero, N. Reeves, V. Pralong, A.R. West, Oxygen Nonstoichiometry and Phase Transitions in $LiMn_{1.5}Ni_{0.5}O_{4-\delta}$, J. Electrochem. Soc. 155 (2008) A282–A291. https://iopscience.iop.org/article/10.1149/1.2832650/meta.